Orientation-Independent-DIC imaging reveals that a transient rise in macromolecular crowding contributes to mitotic chromosome condensation

Shiori Iida [a,b], Satoru Ide [a,b], Sachiko Tamura [a], Tomomi Tani [c], Tatsuhiko Goto[d], Michael Shribak [e*], Kazuhiro Maeshima [a,b*]

[a], Genome Dynamics Laboratory, National Institute of Genetics, Mishima, Shizuoka 411-8540, Japan

[b], Graduate Institute for Advanced Studies, SOKENDAI, Mishima, Shizuoka 411-8540, Japan

[c], Biomedical Research Institute, National Institute of Advanced Industrial Science and Technology (AIST), Ikeda, Osaka 563-8577, Japan

[d], Research Center for Global Agromedicine and Department of Life and Food Sciences, Obihiro University of Agriculture and Veterinary Medicine, Obihiro, Hokkaido 080-8555, Japan

[e], Marine Biological Laboratory, 7 MBL St, Woods Hole, MA 02543, USA.

*To whom correspondence may be addressed. Email: kmaeshim@nig.ac.jp, or mshribak@mbl.edu

Author Contributions: K.M., S. Ide, S. Iida, and M.S. designed the project. M.S. developed OI-DIC microscopy. S. Iida performed OI-DIC imaging, fluorescence imaging, and analyses with the help of S. Ide. S. Iida contributed to scientific illustrations. S.T. performed biochemical experiments and fluorescence imaging. T.G. provided essential resources. T.T. helped OI-DIC imaging. K.M., S. Iida, and M.S. wrote the manuscript with input from all other authors.

Competing Interest Statement: The authors declare that they have no competing interests.

Classification: Biological Science; Cell Biology

Keywords: OI-DIC, mitotic chromosome condensation, macromolecular crowding, chromatin, liquid droplets

This PDF file includes:

Main Text
Figures 1 to 7

Abstract

Genomic information must be faithfully transmitted into two daughter cells during cell division. To ensure the transmission process, interphase chromatin is further condensed into mitotic chromosomes. Although protein factors like condensins and topoisomerase IIα are involved in the assembly of mitotic chromosomes, the physical bases of the condensation process remain unclear. Macromolecular crowding/depletion force, an effective attractive force that arises between large structures in crowded environments around chromosomes, may contribute to the condensation process. To approach this issue, we investigated the "chromosome milieu" during mitosis of living human cells using orientation-independent-differential interference contrast (OI-DIC) module combined with a confocal laser scanning microscope, which is capable of precisely mapping optical path differences and estimating molecular densities. We found that the molecular density surrounding chromosomes increased with the progression from prometaphase to anaphase, concurring with chromosome condensation. However, the molecular density went down in telophase, when chromosome decondensation began. Changes in the molecular density around chromosomes by hypotonic or hypertonic treatment consistently altered the condensation levels of chromosomes. *In vitro*, native chromatin was converted into liquid droplets of chromatin in the presence of cations and a macromolecular crowder. Additional crowder made the chromatin droplets stiffer and more solid-like, with further condensation. These results suggest that a transient rise in macromolecular crowding (proteins and RNAs), likely triggered by the relocation of macromolecules via nuclear envelope breakdown and also by a subsequent decrease in cell-volumes, contributes to mitotic chromosome condensation, shedding light on a new aspect of the condensation mechanism in living human cells.

Significance Statement

Mitotic chromosome condensation is an essential process to transmit replicated chromosomes into two daughter cells during cell division. To study the underlying physical principles of this process, we focused on macromolecular crowding/depletion force, which is a force that attracts large structures in crowded cell environments. Using newly developed special light microscopy, which can image the molecular density of cellular environments, we found that crowding around chromosomes increases during cell division. *In vitro*, higher concentrations of macromolecules condense chromatin and make it stiffer and more solid-like. Our results suggest that the rise in macromolecular crowding renders chromosomes more rigid, ensuring accurate chromosome transmission during cell division.

Introduction

Negatively charged genomic DNA wraps around basic core histone proteins to form nucleosomes. The string of nucleosomes, together with other nonhistone proteins and RNAs, are somewhat irregularly organized in the cell as chromatin (1, 2). During interphase in higher eukaryotic cells, chromatin forms condensed domains as their functional units (3-5). With cell cycle progression, genomic DNA is duplicated by DNA replication and faithfully transmitted into the two daughter cells during mitosis (6, 7). To ensure the transmission process, interphase chromatin is further condensed into mitotic chromosomes. While several players involved in the condensation process, including condensins and topoisomerase IIα, have been identified and extensively investigated (8-13), physical bases of the condensation process remain unclear (14, 15).

In addition to these protein factors, two kinds of physical forces governed by the chromosome milieu may contribute to the condensation process. First, free divalent cations such as Mg^{2+} condense chromatin or chromosomes *in vitro* (16-23), or by computer modeling (24). These cations have long been considered important for local condensation (i.e., nucleosome-nucleosome interactions) because the nucleosomes have a net negative charge and are stretched like "beads on a string" by an electrostatic repulsion force in the absence of cations. Mg^{2+} counters this negative charge and repulsion force. Indeed, a transient increase in free Mg^{2+} is observed during mitosis, contributing to chromosome condensation (25). In addition to Mg^{2+}, acetylation/deacetylation of histone H3 and H4 tails also regulates the electrostatic force between nucleosomes (15, 26).

The other possible physical force is the macromolecular crowding effect/depletion force (27-30). This force may also be critical because the cellular environment is highly crowded with macromolecules such as proteins, RNA, DNA, and others resulting in a molecular density >100 mg/mL. The principle of macromolecular crowding effect/depletion force is simple (Schematic in Fig.1A). Large cellular complexes, like chromatin, are bombarded from all sides by many soluble macromolecules in a crowded environment. When two large complexes come into contact, the macromolecules exert a force equivalent to their osmotic pressure on opposite sides of the two large complexes to keep them together (Schematic in Fig.1A) (27-29). This state is entropically favored because there are more accessible regions after their contact (Schematic in Fig.1A). Indeed, purified nuclei (31) and chromosomes (32) condensed *in vitro* with ~10% (w/v) of long neutral polymers such as polyethylene glycol (PEG) or polyvinyl alcohol. Such high concentrations of a macromolecular "crowder" induced folding of long synthetic chromatin fibers *in vitro* (33). When ~10% of bovine serum albumin (BSA; an anionic protein) was used as a

crowder, condensates of the synthetic chromatin fibers were observed *in vitro* (34). However, it remains unclear whether the macromolecular crowding effect/depletion force is really involved in mitotic chromosome condensation in the cell, especially in higher eukaryotic cells.

To observe the macromolecular crowding effect/depletion force on chromosome condensation, it is essential to measure molecular density in the chromosome milieu of living cells. While it is technically challenging, we gain insight on molecular density by using differential interference contrast (DIC) microscopy (35-38), a standard tool in cell biology research. DIC images are produced by the interference of two laterally displaced light beams passing through a sample (e.g., live cells), capturing information about the optical path length (OPL) in the sample to reveal otherwise invisible features (35). The difference in OPL (optical path difference, OPD) between the two beams contrasts the image, reflecting local differences in the refractive index (RI) within the sample. However, the contrast in DIC images depends on the direction of displacement between the two light beams and the sample, precluding quantitative measurement of the OPL. To overcome the limitations of DIC, Shribak et al. developed an orientation-independent-DIC (OI-DIC) microscopy method (39), which allows the directions of displacement for the two light beams to be rapidly switched by 90º without mechanically rotating the sample or the prisms, generating a quantitative OPD map (Fig. S1). Based on the OPD value, it is possible to estimate the density of intracellular regions in live cells. However, a previous type of OI-DIC with a wide-field epi-fluorescence microscope had difficulty in measuring precise thickness of target structures in the cell (40, 41).

In this study, we have combined a confocal laser scanning microscope (CLSM) with an OI-DIC module (Fig. 1B), which can provide high-resolution maps of OPD by OI-DIC and the thickness of target structures in the cell by CLSM. This new OI-DIC imaging can generate a 3D volume image of the RI and molecular density (dry mass) in living cells based on the calibration data (Fig. 1D(iii)). Using this new OI-DIC system, we quantified the absolute density of the molecules around chromosomes during mitosis of human HCT116 cells. We found that the molecular density surrounding mitotic chromosomes increased with the mitotic progression from prometaphase to anaphase, concurring with chromosome condensation. In telophase, the molecular density decreased as chromosomes began to decondense. Hypertonic treatment of the mitotic cells rapidly increased density and induced chromosome condensation, while hypotonic treatment had the opposite effects. *In vitro*, fiber-like condensates of native chromatin, induced by physiological concentrations of cations, were efficiently converted into chromatin liquid droplets with macromolecular crowders such as PEG, BSA, or Dextran. Additional amounts of crowders made the chromatin droplets stiffer and more solid-like structures. These results suggest that

during mitosis a transient rise in macromolecular crowding (proteins and RNAs) contributes to mitotic chromosome condensation, shedding light on a new aspect of mitotic chromosome condensation in living human cells.

Results

Development of a new OI-DIC system combined with a confocal laser scanning microscope.

To estimate the density of total molecules in the chromosome milieu, we developed a new OI-DIC module combined with a confocal laser scanning microscope (CLSM) (Fig. 1B). We calculated the dry mass density of the sample (Fig. 1D; for more details, see Materials and Methods) based on the OPD map obtained from OI-DIC imaging (e.g., Figs. 1C and S1), the precisely measured thickness (t) of the target structure by CLSM (Figs. 1D, S2C, S4A, and S4C), and the known refractive index (RI) of the surrounding medium. Next, we evaluated whether the new OI-DIC imaging and subsequent analysis could accurately estimate RIs by observing glass rods (diameter = 4 μm) in mineral oils with known refractive indices (RI = 1.54 and 1.58) and calculated the theoretical OPD (Fig. 1C). The theoretical and optically measured OPDs were almost identical (Fig. 1C), validating the accuracy of our new OI-DIC imaging for estimating the RI of samples with measured OPD.

OI-DIC imaging of interphase and mitotic live human HCT116 cells.

Using the procedure described above (Fig. 1D), we performed OI-DIC imaging of interphase and mitotic live human HCT116 cells stably expressing H2B-HaloTag and obtained their OPD maps (Fig. 2A). Riesz images are edge-enhanced OPD maps according to the inverse Riesz transform (42, 43) and are more visually informative with the higher contrast of small details (bottom images, Fig. 2A). Note that asynchronous live cells were used for this imaging to avoid any artifactual effects, such as accumulations and aggregations of proteins and RNAs, caused by the synchronization process. We clearly observed cytoplasmic organelles, nuclear envelopes, and presumably nucleoli in OPD maps of interphase HCT116 cells (Fig. 2A, lower left). In the case of mitotic cells, cytoplasmic organelles, and condensed chromosomes were notable in the Riesz images (Fig. 2A, bottom images). To obtain the thickness measurement (t) of cytoplasm (Figs. 2B, S2A, S2C, and S4A) and chromatin (for nucleoplasm, see Figs. S2B and S2C; for chromosomes, Figs. S4B and S4C) by CLSM, cells were simultaneously labeled with Calcein AM and HaloTag ligand TMR.

Based on the OPDs, thicknesses (t) of cytoplasm and nucleoplasm, and the known RI of the medium (1.3359 for McCoy's 5A including 10% FBS in Fig. 1D(ii)), we calculated the RIs of

cytoplasm (Figs. 2B and S2A) and nucleoplasm (Fig. S2B) in HCT116 cells (Table S1). According to the calibration curve of RIs versus the density of standard solutions for protein or nucleic acid (Fig. 1D(iii)), we obtained total density values in the cytoplasm and nucleoplasm of interphase cells and cytoplasmic density values of various stages of mitotic cells after nuclear envelope breakdown (NEBD) (Fig. 2C). Mitotic stages were judged by their chromosome morphology (Fig. 2A). Also note that we did not look at mitotic chromosomes themselves this time (Fig. 2B) since we wanted to examine molecular crowding around chromosomes, that is, the chromosome milieu.

Molecular crowding in mitotic chromosome milieu is higher than in interphase chromatin. Our quantification (Fig. 2C; Table S1) shows that the density of interphase nucleoplasm is 136 mg/mL, which agrees well with our previous report (40) and is lower than that of cytoplasm (174 mg/mL). Interestingly, the density of cytoplasm in prometaphase cells, which corresponds to chromosome milieu, is 158 mg/mL (Fig. 2C) and higher than that of interphase nucleoplasm. With mitotic progression from prometaphase to anaphase, density gradually increased from 158 mg/mL to 174 mg/mL (Fig. 2C). Maximal cytoplasmic density in anaphase is consistent with previous reports on maximal chromosome compaction in anaphase (44, 45). Once the cytokinesis and chromosome decondensation started at telophase (Fig. 2A), the density was reduced (Fig. 2C). These results suggest that macromolecular crowding in mitotic chromosome milieu is higher than in interphase nucleoplasm and increases with mitotic progression from prometaphase to anaphase.

To further support our findings in HCT116 cells that macromolecular crowding around mitotic chromosomes is higher than in interphase chromatin, we examined another cell line, Indian Muntjac DM cells (Fig. 3A). DM cells were derived from deer fibroblast cells and have very large mitotic chromosomes (46-48). Chromatin and cytoplasm were labeled with Hoechst 33342 and Calcein AM simultaneously (Fig. 3A) to obtain thickness information (t) of interphase cytoplasm (Fig. S2A) and nucleoplasm (Fig. S2B), and mitotic cytoplasm (Fig. S4B).

Using a similar procedure for HCT116 cells, we found that the density of cytoplasm in prometaphase DM cells, which corresponds to chromosome milieu, was 156 mg/mL (Fig. 3B) and higher than that of interphase nucleoplasm (112 mg/mL). Density increased from prometaphase to metaphase (Fig. 3B; Table S2). Obtained results in DM cells were consistent with those in human HCT116 cells, suggesting that a transient rise in the density of chromosome milieu may

be a general feature of mitotic cells. These findings also suggest that macromolecular crowding can contribute to mitotic chromosome condensation.

Density in mitotic chromosomes is 185 mg/mL.

DM cells have much larger and fewer mitotic chromosomes (7-9 chromosomes/cell)(46-48) than HCT116 cells (~46 chromosomes, relatively normal human karyotypes) (49). This difference enabled us to obtain the OPL of mitotic chromosomes (Fig. S4B) and measure the density in mitotic chromosomes as 185 mg/mL in DM cells (left, Fig. S5; Table S2). This value was significantly higher than that of mitotic cytoplasm (164 mg/mL, $p = 0.010$) and comparable to the result of our previous study on the density (208 mg/mL) of the mouse pericentric heterochromatin (chromocenter) (40). However, the density of 185 mg/mL in DM mitotic chromosomes might be underestimated because it was difficult to accurately measure OPL within mitotic chromosomes, even when the chromosomes were larger (Fig. S4B). Also, note that the reported heterochromatin result was obtained using the earlier OI-DIC system that was not installed with CLSM (40), and the thickness (t) estimation of the target structures was not as accurate as the new OI-DIC system.

Hypertonic treatment raised macromolecular crowding and induced chromosome hypercondensation.

We wondered what would happen to the mitotic HCT116 cells and their chromosomes if we changed their cytoplasmic density. To address this question, we first performed the hypertonic treatment with 520 mOsm by adding concentrated phosphate-buffered saline (PBS) (Fig. 4A) as reported in (50, 51), while the physiological osmotic condition is 290 mOsm. Upon hypertonic treatment, the cytoplasmic density increased from 163 mg/mL to 227 mg/mL (Fig. 4B; Table S1). Mitotic chromosomes looked clumped together (Fig. 4A). The signal intensity of mitotic chromatin labeled by H2B-HaloTag-TMR also increased (Fig. 4C), suggesting a rise in macromolecular crowding and induced hypercondensation of mitotic chromosomes upon hypertonic treatment.

Similar findings were achieved using DM cells with hypertonic treatment (Fig. 4D). An increase in cytoplasmic density (Fig. 4E; Table S2) induced hypercondensation of mitotic chromosomes and chromosome clumping (Fig. 4D). In addition, the density within mitotic chromosomes increased from 185 mg/mL to 240 mg/mL (Fig. S5). The cells with a higher density in the cytoplasm tended

to have a higher density for their chromosomes. These results support the hypothesis that macromolecular crowding contributes to mitotic chromosome condensation.

Hypotonic treatment lowered macromolecular crowding and induced chromosome decondensation.

Next, we treated HCT116 cells hypotonically (190 mOsm) by diluting the medium (Fig. 5A). We found that just after the treatment (<10 min), cytoplasmic density in prometa-/metaphase cells reduced from 148 mg/mL to 106 mg/mL (Fig. 5B; Table S1). Chromatin intensity labeled by H2B-HaloTag-TMR also decreased simultaneously (Fig. 5C), suggesting a considerable decondensation of mitotic chromosomes with a reduction in macromolecular crowding. These findings strengthen our notion that macromolecular crowding is involved in mitotic chromosome condensation.

We noticed that the rise in cytoplasmic density recovered >10 min after the hypotonic treatment (Fig. 5B), while cellular effects caused by hypertonic treatment seemed stable after 30 min, consistent with a previous report (52). The induced decondensation of chromosomes also attenuated on the same time scale (Fig. 5A). Interestingly, we found some low-density regions or vesicles in the cytoplasm of prometaphase cells appeared with prolonged hypotonic treatment (>10 min) (shown by arrows in Fig. 5A), suggesting the influx of water molecules were somehow stored and exported to keep intracellular osmotic pressure.

Macromolecular crowders induce liquid droplets of chromatin *in vitro*, and additional crowding make the droplets stiffer and more solid-like.

To finally examine how an increase in macromolecular crowding during mitosis can change the physical properties of chromosomes, we performed an *in vitro* condensation assay using chicken native chromatin. The peak size of the native chromatin used for this assay was ~6 kb and corresponded to ~30 nucleosomes (Fig. S6A, B). Cations diminish the repulsion between negatively charged nucleosomes in the chromatin and electrostatically attract them to form chromatin condensates (19-23, 25, 51, 53, 54). Therefore, we incubated our native chromatin in a buffer containing 100 mM K^+ and 0.8 mM Mg^{2+} to mimic physiological concentrations of cations in the cell (25) and found many fiber-like condensates of chromatin were formed (Fig. 6A, Panel 1), consistent with previous reports (25, 51, 54, 55).

We simulated macromolecular crowding of chromosome milieu by incubating increasing concentrations of polyethylene glycol (a neutral polymer; PEG, M.W. ~8 kDa), bovine serum albumin (BSA, M.W. 66 kDa), or Dextran (M.W. ~200kDa) with our fiber-like condensates of

chromatin. We first added increasing concentrations of PEG as a crowder and observed morphological changes of chromatin condensates. With 10 mg/mL (w/v) (corresponding to 1.25 mM) PEG, some spherical structures were found among fibrous condensates (Fig. 6A, Panel 2). At 20 mg/mL (2.5 mM) PEG, almost all condensates became spherical with various sizes and looked like liquid droplets formed by liquid-liquid phase separation (LLPS) (Fig. 6A, Panel 3) (53, 55-57). Indeed, the droplets often fused to form larger droplets (Fig. 6B; Movie S1). Upon increase in PEG to 40 mg/mL (5.0 mM), droplets were connected to one another (Fig. 6A, Panel 4). Note that their sizes were not as large as those with 20 mg/mL PEG (Fig. 6A, right). These were presumably stuck together and not fused into lager droplets during our observation period (up to 1 h). Results using a higher concentration of PEG suggested further condensation of chromatin creates stiffer and more solid-like droplets, reducing their fluidity (Fig. 6D).

Next, we used BSA as another crowder in the same concentration of cations and native chromatin. BSA affected chromatin morphology at higher concentrations (w/v) than PEG. At 50 mg/mL (0.75 mM) BSA, chromatin droplets formed among fibers (Fig. 6C, Panel 2). Almost all condensates became droplets at 100 mg/mL (1.5 mM) BSA (Fig. 6C, Panel 3). As in the case of PEG, increasing the BSA concentration to 200 mg/mL (3.0 mM) formed clusters of droplets that appeared to stick together (Fig. 6C, Panel 4). Again, their sizes were smaller than those with 100 mg/mL (1.5 mM) BSA due to much fewer fusion events being prevented by stiffer and more solid-like properties (Fig. 6C, right). We also obtained a similar set of results using Dextran (M.W. ~200kDa) (Fig. S6C). These results suggest that macromolecular crowding can change the physical properties of chromosomes. Addition of crowders induced the formation of chromatin liquid droplets *in vitro*. Further crowding pushed chromatin droplets from the outside, condensed chromatin, and increased droplet stiffness, which may have prevented droplet fusions at our time scale (up to 1 h) due to the reduced fluidity (Fig. 6D).

To examine whether the chromatin droplet formation induced by macromolecular crowding was reversible, we lowered the crowding effect around the droplets. After droplets were made using 20 mg/mL PEG, 100 mg/mL BSA, or 50 mg/mL Dextran, the droplet solutions were diluted 10-fold with a buffer containing 100 mM K^+ and 0.8 mM Mg^{2+} with or without crowder (Figs. 6E, F and S6D). The number of droplets in the diluted buffer without crowder substantially decreased and more small chromatin condensates appeared as compared to the control droplets in the diluted buffer with crowder. Droplets resolved into small chromatin condensates, suggesting that droplet formation by macromolecular crowding is reversible.

Discussion

The chromosome milieu governs physical forces contributing to chromosome condensation. We developed a novel OI-DIC microscopy system combined with CLSM to elucidate the effects of the chromosome milieu in live mitotic cells (Fig. 1B). The subsequent analysis enabled the absolute density in cytoplasm of various stages of mitotic human cells to be calculated, as well as in the cytoplasm and nucleoplasm of interphase cells. We demonstrated that the density of cytoplasm in metaphase cells (163 mg/mL) was higher than that of interphase nucleoplasm (136 mg/mL). Density gradually increased from 158 mg/mL to 174 mg/mL (Fig. 2C) as cells mitotically progressed from prometaphase to anaphase, concurring with chromosome condensation (44, 45). Furthermore, hypertonic treatment of the mitotic cells rapidly raised density and induced chromosome condensation, while hypotonic treatment had the opposite effects. Our findings suggest that a transient rise in macromolecular crowding (the density of proteins and RNAs) during mitosis is involved in mitotic chromosome condensation, providing a novel insight into the physical bases of mitotic chromosome condensation in living human cells.

To our knowledge, we are the first to demonstrate that the macromolecular crowding/depletion force converts fibrous chromatin condensates formed by cations into liquid droplets *in vitro*. Previous reports on chromatin liquid droplet formation have thus far only used synthetic nucleosomes such as 12-mer arrays, which have uniform properties in the length, spacing, size, and modifications (51, 53, 58). The liquid droplets we observed using native chromatin reminded us of the chromatin liquid droplets in living mitotic cells when Schneider et al. injected cells with the restriction enzyme AluI to fragment chromatin (15). Increasing macromolecular crowding *in vitro* made the droplets stiffer and more solid-like, with further chromatin condensation (Fig. 6D). While cations induced an electrostatic attraction force between chromatin, the macromolecular crowding/depletion force worked as external pressure from outside (Fig. 6D). Our results suggest that the macromolecular crowding/depletion force is another force that contributes to chromosome rigidity during mitosis (Fig. 7). The additional condensation by increased macromolecular crowding is particularly advantageous for the chromosome segregation and transmission processes during anaphase, when mechanical shearing stress is high. Note that the highest cytoplasmic density level was identified in anaphase (Fig. 2C) and concurred with previous reports of the highest level of chromosome compaction in anaphase (44, 45). Condensed chromatin domains in interphase have been observed in a variety of cells (59-63) and are proposed to work as building blocks for mitotic chromosomes (5, 61). The assembled stiffer chromatin droplets that we observed in the highly crowding situation looked like mitotic chromosomes (Panels 4 in Fig. 6A and C and Fig. S6C). Hence, the macromolecular

crowding/depletion force may facilitate the assembly of condensed chromatin domains to form mitotic chromosomes.

What is the underlying mechanism of upregulating macromolecule density during mitosis? While small molecules are rather evenly distributed within the cell, macromolecules such as proteins, RNAs, and DNAs in eukaryotic cells are highly compartmentalized in interphase by nuclear membrane (left, Fig. 7; Fig. 2A). We propose that cells regulate their density localizations by compartmentalization and can upregulate cytoplasmic density after NEBD (right, Fig. 7). OPD maps of interphase cells show that cytoplasmic organelles (ER, Golgi apparatus, mitochondria, etc.), the nuclear membrane structure, and nucleoli are prominent high-density structures (bottom left, Fig. 2A). Upon NEBD, the nuclear envelope, nuclear pore complexes, nuclear lamina, and nucleoli are disassembled into small pieces (complexes or vesicles) for cell division and become a part of the "chromosome milieu." As a result, cytoplasmic and nucleolus factors are exposed to chromosomes and fully contribute to an increase in macromolecular crowding (right, Fig. 7). For instance, nucleoli, which are enriched with proteins and RNAs, occupy ~12% of the nuclear volume and have a high density of >200 mg/mL (Fig. S3; (40)). Ribosomes and some of the nucleolar components also locate to the chromosome periphery (e.g., (64-66)). Together, these fully coordinated mitotic events can lead to a transient rise in macromolecular crowding observed during mitosis (right, Fig. 7).

A transient rise in macromolecular crowding during mitosis can act as an additional force to form larger chromosomes in higher eukaryotic cells. Higher eukaryotic cells have a mitotic process called open mitosis. NEBD occurs during prophase, and the nuclear envelope is regenerated around the chromosomes in telophase (6, 7). Our findings suggest that the open mitosis system allows the cell to upregulate macromolecular crowding during mitosis. Closed mitosis occurs in the case of lower eukaryotes (e.g., fungi and yeasts), where the nuclear envelope does not break down during mitosis (67, 68). Their "chromosome milieu" seems constant during mitosis, suggesting that eukaryotic organisms might have evolved to acquire open mitosis and an additional chromosome compaction force for their larger chromosomes. As discussed above, this force could be beneficial to make larger chromosomes more rigid to ensure faithful transmission into daughter cells.

Our model described above (Fig. 7) is well compatible with reports by Son et al. (69) and Zlotek-Zlotkiewicz et al. (70), who measured the volume and density dynamics in proliferating mammalian cells. They found a rapid increase in cell volume and a decrease in whole cell density just as cells entered prophase. This prophase cell swelling seems to be driven by an osmotic

water exchange (69), possibly to generate a larger, rounder space to promote accurate and rapid chromosome segregation in the context of animal tissue (69). Subsequently, cell volume decreased in the metaphase-anaphase transition. The reduction of cell volume can also contribute to an increase in molecular density with the mitotic progression from prometaphase to anaphase (Fig. 2C), promoting further chromosome condensation during mitosis, as shown in (44, 45, 71). Furthermore, our finding is consistent with data from an intracellular crowding sensor GimRET (72). A transient rise in the GimRET signal during cell division of HeLa cells (Fig. S8 in (72)) suggested an up-regulation of macromolecular crowding during the chromosome condensation process.

The new OI-DIC module combined with CLSM can obtain matched high-resolution OPD and confocal images to get precise absolute densities in live cells, while another density microscopy (73) may have difficulty because it requires a separate reference beam and uses two objective lenses for OPD/RI reconstruction. The new OI-DIC imaging system offers fresh insight into the density of live cellular environments, which govern the functions of protein/RNA factors and their complexes via their diffusions.

Materials and Methods

Description of OI-DIC/confocal setup.

A simplified optical schematic of the confocal laser scanning microscope Olympus FV3000 (Evident, Tokyo, Japan) with the OI-DIC module is shown in Fig. 1B. The FV3000 consists of an inverted microscope Olympus IX83, a confocal scan unit, and a laser combiner. The microscope IX83 was equipped with a 100-W halogen lamp U-LH100L-3, a bandpass filter 546/10 nm (Chroma, Bellows Falls, VT, USA), a condenser IX2-DICD with front lens U-TLD 0.9NA, a water immersion objective lens UPlanSApo 60x/1.2NA W, and an 8-positions mirror turret FV30-RFACA. The condenser, objective lens, and specimen under investigation were placed in a Thermo Box IX83TB (Tokai Hit, Shizuoka, Japan). The turret contains an LSM mirror and analyzer cube IX3-FDICT. Regular Olympus DIC sliders were replaced by custom beam-shearing DIC assemblies. The first assembly consists of a pair of DIC prisms U-ODIC100HR, a liquid crystal polarization rotator, and a liquid crystal variable retarder (ARCoptix, Neuchatel, Switzerland). The second assembly consists of a pair of DIC prisms U-DICTHR and a liquid crystal polarization rotator. The assemblies can quickly switch the shear direction by 90º and change the bias without any mechanical movement. A set of 4 or 6 DIC images was captured by a digital camera Infinity 3-1M (Lumenera, Ottawa, Canada). More details about OI-DIC image acquisition and processing were described previously (40, 43). The laser combiner has four laser diodes with wavelengths of 405 nm, 488 nm, 562 nm, and 640 nm. Their beam intensities were controlled by an acousto-optic tunable filter and then delivered by a single-mode optical fiber to a confocal scan unit. Excitation dichroic mirror reflects the laser light to a pair of Galvano scanning mirrors and CLSM mirror. The emission light is transmitted by the dichroic mirror to an adjustable confocal pinhole and 2-channel multi-alkali PMT spectral detector unit FV31-SD. The spectral detector employs efficient Volume Phase Holographic transmission grating and adjustable slit with 1–100 nm bandwidth from a 400–800 nm detection region.

OI-DIC imaging of glass rods.

A small number of glass rods 4 μm in diameter were suspended in two types of mineral oil with refractive indices of 1.54 and 1.58. Approximately 2 μL of the suspended solution was sandwiched between a glass slide and a coverslip and then sealed with nail polish. The glass rods in the mineral oil were analyzed by OI-DIC microscopy using the same procedure as the live cell imaging. A plot of the intensity profile across a glass rod was created by ImageJ (line width: 10 pixels) to validate density imaging by OI-DIC microscopy. The theoretical OPD curve was

calculated based on the thickness and the RI of a glass rod, assuming that the cross-section of the glass rod is a circle with a diameter of 4 μm.

Cell lines and establishment of stable cell lines.

HCT116 cells (CCL-247; ATCC) were cultured at 37 °C and 5% CO_2 in McCoy's 5A medium (SH30200.01; HyClone) supplemented with 10% fetal bovine serum (FBS; FB-1061/ 500; Biosera). Indian Muntjac DM cells were a generous gift from Dr. H. Kimura and Dr. P. Cook (Tokyo Tech and Oxford University, respectively) (47). The cells were cultured at 37 °C and 5% CO_2 in Dulbecco's Modified Eagle's medium (DMEM; D5796- 500ML; Sigma-Aldrich) supplemented with 20% FBS.

The transposon system was used to stably express H2B-Halo in the HCT116 cell line. The constructed plasmid pPB-CAG-IB-H2B-HaloTag (41) was cotransfected with pCMV-hyPBase (provided by Sanger Institute with a materials transfer agreement) into HCT116 cells with the Effectene transfection reagent kit. Transfected cells were then selected with 10 μg/mL blasticidin S. HCT116 cells expressing SMC2-mAID-mClover and Tet-OsTIR1 were used as parental cells (74, 75).

pPB-CAG-mCherry-NPM1 plasmid was constructed on the basis of pPB-CAG-IB (provided from Sanger Institute with a materials transfer agreement). Full length NPM1 fused to EGFP at the N-terminus was cloned into pEF1-FRT plasmid (76). From pEF1-EGFP-NPM1-FRT, the coding region of NPM1 was amplified using the following primer pairs: 5'-GACGAGCTGTACAAGGGTGGAGGTGGATCTGGTGGAG-3' and 5'-GGGGCGGAATTCGTTTTAAAGAGACTTCCTCCACTGCCAG-3'. The mCherry fragment was amplified from pmCherry_a_tubulin_IRES_puro2 (#21043, Addgene) using the following primers: 5'- GAATTGATCTCTCGAGATGGTGAGCAAGGGCGAGGAG-3' and 5'-CTTGTACAGCTCGTCCATGCC-3'. The amplified fragments were joined together using standard overlapping PCR and inserted into pPB-CAG-IB-H2B-HaloTag digested with XhoI and HpaI using In-Fusion (639650; Takara). To stably express mCherry-NPM1 in HCT116 cell line, the transposon system was used. The constructed plasmid pPB-CAG-mCherry-NPM1 was cotransfected with pCMV-hyPBase into HCT116 cells expressing mAID-mClover-RPA194 (77) with the Neon Electroporation System (MPK5000; Thermo Fisher Scientific). For the electroporation, cells were resuspended in Neon Resuspension Buffer R (10 μL, Neon kit, Invitrogen) to a final concentration of 2.5×10^7 cells/mL and mixed with 500 ng of pPB-CAG-mCherry-NPM1 and pCMV-hyPBase, respectively. The mixture was pulsed once with a voltage of

1400 and a width of 20. Transfected cells were then selected with 10 μg/mL blasticidin S (029–18701; Wako).

Cell preparation.

Cells were seeded on 24 mm × 24 mm square glass coverslips coated with 2.5 μg/mL fibronectin (354008; Corning) diluted in PBS for 1 h at 37 °C and cultured for 1–2 days. In HCT116 cells, cytoplasm and histone H2B-Halo were labeled with 3 μg/mL Calcein-AM and 5 nM TMR, respectively, for 30 min at 37 °C in 5% CO_2, then washed with 1× HBSS (H1387; Sigma-Aldrich) three times. In DM cells, DNA was stained with 1.8 μg/mL Hoechst33342 (H342; Dojindo) instead of TMR. Cells were then incubated in the following phenol red-free media. HCT116 cells were observed in McCoy's 5A (1-18F23-1; BioConcept) with 10% FBS, and DM cells were observed in DMEM (21063-029; Thermo Fisher Scientific) with 20% FBS. The cells were mounted on a glass slide with a silicone spacer having a thickness of 0.5 mm. We observed the mounted cells by OI-DIC and fluorescence imaging. Cells were not synchronized.

Live-cell OI-DIC microscopy imaging.

Before the experiment, the Thermo Box was set at 37 °C. The specimen was placed on the microscope stage, and the microscope was switched to the DIC mode. The analyzer was in the beam path, and the LSM mirror was out. The camera showed a live DIC image. The objective lens was focused on the middle plane of the cell under investigation. Using the custom software, which controlled the beam-shearing assemblies, we captured a set of DIC images with X- and Y-shear directions. We took 3 images in each direction, with zero and ±0.15λ biases. The total acquisition time of six images was about 1 s. The corresponding background image without cells or structures was also taken prior to each image acquisition to create the OPD map. The captured images were processed according to the previously reported algorithm (43), and the OPD map was generated (40) (Fig. S1). In the next step, the microscope was switched to the confocal mode. The analyzer was out of the beam path, and the LSM mirror was in. Then, we captured the z-stack and found the thickness of the cell, t.

Measurement of the Refractive Index (RI) of standard solutions.

To obtain calibration curves of the RIs of proteins and nucleic acids (Fig. 1D (iii)), bovine serum albumin (BSA; Sigma; A9647-100G) and salmon sperm DNA (WAKO; 043-31381) were dissolved in water at concentrations of 0–200 and 0–30 mg/mL, respectively. The RIs of the prepared standard solutions were measured with a refractometer, Abbé-3L (Bausch & Lomb). The measured RIs and solution densities were plotted and fitted with linear functions to obtain

calibration curves. RI of the medium was also measured by the same refractometer. The RI of McCoy's 5A/10% FBS was 1.3359 and the RI of DMEM/20% FBS was 1.3373.

Density estimation of cellular contents.

This OI-DIC version allowed the OI-DIC image and confocal images to be obtained in the same field of view. Therefore, it was possible to estimate both the OPD and thickness at a particular point and obtain an accurate molecular density at that point. The OPD was proportional to the thickness of a sample and the difference in RI between the sample and the surrounding solution, as shown in Fig. 1D(i). Therefore, we calculated the RI of samples based on the RI of the surrounding solution and sample thickness.

First, we cropped the OPD map to manually match the field of the confocal image captured by CLSM using intracellular structures (e.g., nuclei) as indicators. Second, to calculate the Optical Path Difference (OPD) between medium and samples, we obtained the Optical Path Length (OPL) of medium, OPLmed, (the mean OPL of 5 ROIs [a circle with a diameter of ~0.6 μm] outside of cells) and OPL of sample, OPLs, at the selected points within the sample. We calculated OPD as the difference between OPLs and OPLmed. We got the thickness of the sample at the same points we obtained the OPD using the corresponding confocal image. The thickness threshold was set at the specific point of the difference between the maximum and minimum intensity of the z-axis profile of the selected points (also see Figs. S2C, S4A, and S4C). Then, we calculated the dry mass density ("density" for short) of the cytoplasm using the following formula:

$$RIs = RImed + OPD/t,$$

where RImed is the refractive index of the surrounding medium.

RImed was measured as 1.3359 (McCoy's 5A/10% FBS) and 1.3373 (DMEM/20% FBS). We determined the density of the sample from its RI using our calibration curves (Fig. 1D(iii); $RI = 1.333 + 1.65 \times 10^{-4} \times C$, where C is density). Also see "Measurement of Refractive Index (RI) of standard solutions"; Figs. 1D, 2B, and S2A.

To identify the density of the nucleus or the chromosomes, we calculated the OPD of the nucleus and cytoplasm, OPDnu-cy, and the OPD of chromosomes and cytoplasm, OPDch-cy in all the combination pairs of the selected points at cytoplasm and nucleus or chromosomes and obtained the average OPDnu-cy or OPDch-cy at each specific point. We corrected cytoplasm thickness as shown in Figs. S2B and S4B. All measurements were done using FIJI software.

Hypertonic and hypotonic treatment.

For hypertonic treatment, cells were incubated in a medium supplemented with 0.9 mL DMEM and 0.1 mL 10X PBS just before observation. Cells were observed by OI-DIC within 1 h. For hypotonic treatment, cells were incubated in a medium supplemented with 1 mL DMEM and 1 mL MilliQ water just before observation. Cells were observed by OI-DIC within 1 h.

Chromatin/DNA compaction analysis.

To quantify DNA density, we used the obtained confocal images. In a central z-section of a mitotic cell (determined by visual inspection based on the largest area of cytoplasm), the DNA channel was denoised using a Gaussian blur filter ($\sigma = 2$) and threshold set using the Otsu dark method in FIJI. The resulting binary mask was converted into a selection, and the DNA mean fluorescence within this ROI was measured. All data points were normalized to the mean of unperturbed control cells. For hypotonic treatment, only images taken within 10 min after treatment were used.

Chromatin preparation and condensation/droplet formation assay, and the droplet imaging.

Fresh chicken blood was obtained from the wing vein of Tosa-jidori. Preparation of chicken native chromatin was as described previously (54). Briefly, 2 mL of fresh chicken blood was lyzed with 20 mL of MLB (60 mM KCl, 15 mM NaCl, 15 mM HEPES-KOH (pH 7.3), 2 mM $MgCl_2$, 0.1% NP-40, and 1 mM phenyl-methylsulfonyl fluoride [PMSF]) for 10 min on ice. After centrifugation at 1200 × g at 4 °C for 5 min, the supernatant was removed and resuspended in 20 mL of MLB. This step was repeated four times before the samples were ready for chromatin purification. Chromatin purification was carried out as described by (78), with some modifications. The nuclei (equivalent to ~2 mg of DNA) in nuclei isolation buffer (10 mM Tris-HCl, pH 7.5, 1.5 mM $MgCl_2$, 1.0 mM $CaCl_2$, 0.25 M sucrose, 0.1 mM PMSF) were digested with 50 U of micrococcal nuclease (Worthington, Lakewood, NJ) at 30 °C for 2 min. The reaction was stopped by adding ethylene glycol tetraacetic acid (EGTA) to a final concentration of 2 mM. After being washed with nuclei isolation buffer, the nuclei were lyzed with lysis buffer (10 mM Tris-HCl (pH 8.0), 5 mM EDTA, 0.1 mM PMSF) on ice for 5 min. The lysate was dialyzed against dialysis buffer (10 mM HEPES-NaOH (pH 7.5), 0.1 mM EDTA, 0.1 mM PMSF) at 4 °C overnight using Slide-A-Lyzer (66380 Thermo Scientific). The dialyzed lysate was centrifuged at 20400 × g at 4 °C for 10 min. The supernatant was recovered and used as the purified chromatin fraction. The purity and integrity of the chromatin protein components were verified by 14% SDS–PAGE (Fig. S6A). To examine the average DNA length of the purified chromatin, DNA was isolated from the chromatin fraction and electrophoresed in a 0.7% agarose gel (Fig. S6B).

Samples of chicken chromatin (4 μg) were incubated with 10 mM HEPES-NaOH (pH 7.5), 0.8 mM $MgCl_2$, 100 mM KCl, and indicated concentration of crowder in 200 μL of a reaction mixture at room temperature for 30 min. The mixture (10 μL) was mounted on a glass slide with 2 μL of DAPI solution (82 μg/mL). The coverslips were sealed with nail polish. The crowders used were polyethylene glycol (PEG; P5413, Sigma-Aldrich), Dextran (180~210 kDa, 041-22612, Fujifilm), and bovine serum albumin (BSA; BAC65, Equitech-Bio, Inc), and first dissolved in a buffer containing 10 mM HEPES-NaOH (pH 7.5) and 0.1 mM EDTA as 30% (w/v) solution. ImageJ was used to measure the droplet diameter by converting droplet images to binary images with a threshold of 80-255. Droplet diameters were then measured using "Analyze Particles".

For the chromatin assays at 40 mg/mL PEG, 200 mg/mL BSA, or 100 mg/mL Dextran (Panel 4 in Figs. 6A, 6C, and S6C), the chromatin droplets were first formed at 20 mg/mL PEG, 100 mg/mL BSA, or 50 mg/mL Dextran, and then additional crowder was added.

For the droplet dilution assays (Fig. 6D), chromatin droplets were first formed at 20 mg/mL PEG, 100 mg/mL BSA, or 50 mg/mL Dextran. Then, 9 volumes of a dilution buffer containing 10 mM HEPES-NaOH (pH 7.5), 0.8 mM $MgCl_2$, 100 mM KCl with or without crowder were added, incubated for 3 h and mounted with DAPI as described above.

For the chromatin droplet imaging, optical sectioning images were recorded with a 200 nm step size using a DeltaVision microscope (Applied Precision) and deconvolved to remove out-of-focus information. Projected images from five sections were shown as described previously (23).

Acknowledgments

We are grateful to Dr. K.M. Marshall for critical reading and editing of this manuscript and Dr. R. Imai for a preliminary result on density in mitotic chromosomes. We thank Dr. M. Kanemaki for providing their HCT116 cell line, Dr. H. Kimura and Dr. P. Cook for providing their DM cell line, Dr. Y. Murayama, Dr. A. Nakano, Dr. K. Hibino, Mr. M. A. Shimazoe, and Maeshima laboratory members for their helpful discussions and support. This work was supported by JSPS grants JP21H02453 (K.M.), JP22H05606 (S.Ide), JP21H02535 (S.Ide), JP20H05936 (K.M.), JP23K17398 (K.M., S.Ide, T.T.), Takeda Science Foundation, Inoué Endowment Fund (M.S.) and NIGMS/NIH grant R01GM101701 (M.S.). S.Iida was a SOKENDAI Special Researcher (JST

SPRING JPMJSP2104) and supported by a SOKENDAI Genetics Course travel fellowship. S.Iida is currently a JSPS Fellow (JP23KJ0996).

References

1. T. Misteli, The Self-Organizing Genome: Principles of Genome Architecture and Function. Cell 183, 28-45 (2020).
2. K. Maeshima, S. Iida, S. Tamura, Physical Nature of Chromatin in the Nucleus. Cold Spring Harb Perspect Biol 13 (2021).
3. S. S. Rao et al., A 3D map of the human genome at kilobase resolution reveals principles of chromatin looping. Cell 159, 1665-1680 (2014).
4. L. Mirny, J. Dekker, Mechanisms of Chromosome Folding and Nuclear Organization: Their Interplay and Open Questions. Cold Spring Harb Perspect Biol 14 (2022).
5. K. Maeshima, S. Iida, M. A. Shimazoe, S. Tamura, S. Ide, Is euchromatin really open in the cell? . Trends in Cell Biology 10.1016/j.tcb.2023.05.007 (2023).
6. B. Alberts et al., Molecular Biology of the Cell, Seventh Edition (2022).
7. T. D. Pollard, W. C. Earnshaw, J. Lippincott-Schwartz, G. Johnson, Cell Biology, 4th Edition. (2022).
8. T. Hirano, Condensin-Based Chromosome Organization from Bacteria to Vertebrates. Cell 164, 847-857 (2016).
9. J. R. Paulson, D. F. Hudson, F. Cisneros-Soberanis, W. C. Earnshaw, Mitotic chromosomes. Semin Cell Dev Biol 117, 7-29 (2021).
10. F. Uhlmann, SMC complexes: from DNA to chromosomes. Nat Rev Mol Cell Biol 17, 399-412 (2016).
11. P. Batty, D. W. Gerlich, Mitotic Chromosome Mechanics: How Cells Segregate Their Genome. Trends Cell Biol 29, 717-726 (2019).
12. C. F. Nielsen, T. Zhang, M. Barisic, P. Kalitsis, D. F. Hudson, Topoisomerase IIalpha is essential for maintenance of mitotic chromosome structure. Proc Natl Acad Sci U S A 117, 12131-12142 (2020).
13. I. F. Davidson, J. M. Peters, Genome folding through loop extrusion by SMC complexes. Nat Rev Mol Cell Biol 22, 445-464 (2021).
14. A. E. C. Meijering et al., Nonlinear mechanics of human mitotic chromosomes. Nature 605, 545-550 (2022).
15. M. W. G. Schneider et al., A mitotic chromatin phase transition prevents perforation by microtubules. Nature 10.1038/s41586-022-05027-y (2022).
16. M. P. Marsden, U. K. Laemmli, Metaphase chromosome structure: evidence for a radial loop model. Cell 17, 849-858 (1979).
17. W. C. Earnshaw, U. K. Laemmli, Architecture of metaphase chromosomes and chromosome scaffolds. J Cell Biol 96, 84-93 (1983).
18. D. F. Hudson, P. Vagnarelli, R. Gassmann, W. C. Earnshaw, Condensin is required for nonhistone protein assembly and structural integrity of vertebrate mitotic chromosomes. Dev Cell 5, 323-336 (2003).
19. J. Widom, Physicochemical studies of the folding of the 100 A nucleosome filament into the 300 A filament. Cation dependence. J Mol Biol 190, 411-424 (1986).
20. B. Dorigo, T. Schalch, K. Bystricky, T. J. Richmond, Chromatin fiber folding: requirement for the histone H4 N-terminal tail. J Mol Biol 327, 85-96 (2003).
21. A. Allahverdi et al., The effects of histone H4 tail acetylations on cation-induced chromatin folding and self-association. Nucleic Acids Res 39, 1680-1691 (2011).
22. S. Pepenella, K. J. Murphy, J. J. Hayes, A distinct switch in interactions of the histone H4 tail domain upon salt-dependent folding of nucleosome arrays. J Biol Chem 289, 27342-27351 (2014).

23. K. Maeshima et al., Nucleosomal arrays self-assemble into supramolecular globular structures lacking 30-nm fibers. EMBO J 35, 1115-1132 (2016).
24. H. H. Gan, T. Schlick, Chromatin ionic atmosphere analyzed by a mesoscale electrostatic approach. Biophys J 99, 2587-2596 (2010).
25. K. Maeshima et al., A Transient Rise in Free Mg(2+) Ions Released from ATP-Mg Hydrolysis Contributes to Mitotic Chromosome Condensation. Curr Biol 28, 444-451 e446 (2018).
26. A. Zhiteneva et al., Mitotic post-translational modifications of histones promote chromatin compaction in vitro. Open Biol 7 (2017).
27. S. Asakura, F. Oosawa, On interaction betweentwo bodies immersed in a solution of macromolecules. J Chem Phys 22, 1255—1256 (1954).
28. D. Marenduzzo, K. Finan, P. R. Cook, The depletion attraction: an underappreciated force driving cellular organization. J Cell Biol 175, 681-686 (2006).
29. R. Hancock, The crowded nucleus. Int Rev Cell Mol Biol 307, 15-26 (2014).
30. M. Delarue et al., mTORC1 Controls Phase Separation and the Biophysical Properties of the Cytoplasm by Tuning Crowding. Cell 174, 338-349.e320 (2018).
31. R. Hancock, Packing of the polynucleosome chain in interphase chromosomes: evidence for a contribution of crowding and entropic forces. Semin Cell Dev Biol 18, 668-675 (2007).
32. R. Hancock, Structure of metaphase chromosomes: a role for effects of macromolecular crowding. PLoS One 7, e36045 (2012).
33. A. Zinchenko, N. V. Berezhnoy, Q. Chen, L. Nordenskiold, Compaction of Single-Molecule Megabase-Long Chromatin under the Influence of Macromolecular Crowding. Biophys J 114, 2326-2335 (2018).
34. A. Zinchenko, Q. Chen, N. V. Berezhnoy, S. Wang, L. Nordenskiold, Compaction and self-association of megabase-sized chromatin are induced by anionic protein crowding. Soft Matter 16, 4366-4372 (2020).
35. R. D. Allen, G. B. David, G. Nomarski, The zeiss-Nomarski differential interference equipment for transmitted-light microscopy. Z Wiss Mikrosk 69, 193-221 (1969).
36. E. D. Salmon, P. Tran, High-resolution video-enhanced differential interference contrast (VE-DIC) light microscopy. Methods Cell Biol 56, 153-184 (1998).
37. S. Inoué, The role of microtubule assembly dynamics in mitotic force generation and functional organization of living cells. J Struct Biol 118, 87-93 (1997).
38. R. Oldenbourg, Polarized light microscopy: principles and practice. Cold Spring Harb Protoc 2013 (2013).
39. M. Shribak, Quantitative orientation-independent differential interference contrast microscope with fast switching shear direction and bias modulation. J Opt Soc Am A Opt Image Sci Vis 30, 769-782 (2013).
40. R. Imai et al., Density imaging of heterochromatin in live cells using orientation-independent-DIC microscopy. Mol Biol Cell 28, 3349-3359 (2017).
41. R. Nagashima et al., Single nucleosome imaging reveals loose genome chromatin networks via active RNA polymerase II. J Cell Biol 218, 1511-1530 (2019).
42. K. G. Larkin, P. A. Fletcher, Isotropic scalar image visualization of vector differential image data using the inverse Riesz transform. Biomed Opt Express 5, 907-920 (2014).
43. M. Shribak, K. G. Larkin, D. Biggs, Mapping optical path length and image enhancement using quantitative orientation-independent differential interference contrast microscopy. J Biomed Opt 22, 16006 (2017).
44. F. Mora-Bermudez, D. Gerlich, J. Ellenberg, Maximal chromosome compaction occurs by axial shortening in anaphase and depends on Aurora kinase. Nat Cell Biol 9, 822-831 (2007).
45. Z. Liang et al., Chromosomes progress to metaphase in multiple discrete steps via global compaction/expansion (stress) cycles. Cell 161, 1124–1137 (2015).
46. S. Hihara et al., Local nucleosome dynamics facilitate chromatin accessibility in living mammalian cells. Cell Rep 2, 1645-1656 (2012).

47. E. M. Manders, H. Kimura, P. R. Cook, Direct imaging of DNA in living cells reveals the dynamics of chromosome formation. J Cell Biol 144, 813-821 (1999).
48. C. Hoencamp et al., 3D genomics across the tree of life reveals condensin II as a determinant of architecture type. Science 372, 984-989 (2021).
49. S. Iida et al., Single-nucleosome imaging reveals steady-state motion of interphase chromatin in living human cells. Science Advances. 8, eabn5626 (2022).
50. H. Albiez et al., Chromatin domains and the interchromatin compartment form structurally defined and functionally interacting nuclear networks. Chromosome Res 14, 707-733 (2006).
51. H. Strickfaden et al., Condensed Chromatin Behaves like a Solid on the Mesoscale In Vitro and in Living Cells. Cell 183, 1772-1784 e1713 (2020).
52. A. Burgess, M. Rasouli, S. Rogers, Stressing mitosis to death. Front Oncol 4, 140 (2014).
53. B. A. Gibson et al., Organization of Chromatin by Intrinsic and Regulated Phase Separation. Cell 179, 470-484 e421 (2019).
54. Y. Itoh et al., 1,6-hexanediol rapidly immobilizes and condenses chromatin in living human cells. Life Sci Alliance 4, e202001005 (2021).
55. A. A. Hyman, C. A. Weber, F. Julicher, Liquid-liquid phase separation in biology. Annual review of cell and developmental biology 30, 39-58 (2014).
56. S. F. Banani, H. O. Lee, A. A. Hyman, M. K. Rosen, Biomolecular condensates: organizers of cellular biochemistry. Nat Rev Mol Cell Biol 18, 285-298 (2017).
57. Y. Shin, C. P. Brangwynne, Liquid phase condensation in cell physiology and disease. Science 357 (2017).
58. B. A. Gibson et al., In diverse conditions, intrinsic chromatin condensates have liquid-like material properties. Proc Natl Acad Sci U S A 120, e2218085120 (2023).
59. A. S. Belmont, K. Bruce, Visualization of G1 chromosomes: a folded, twisted, supercoiled chromonema model of interphase chromatid structure. J Cell Biol 127, 287-302 (1994).
60. N. Kireeva, M. Lakonishok, I. Kireev, T. Hirano, A. S. Belmont, Visualization of early chromosome condensation: a hierarchical folding, axial glue model of chromosome structure. J Cell Biol 166, 775-785 (2004).
61. T. Nozaki et al., Dynamic Organization of Chromatin Domains Revealed by Super-Resolution Live-Cell Imaging. Mol Cell 67, 282-293 e287 (2017).
62. J. Xu et al., Super-Resolution Imaging of Higher-Order Chromatin Structures at Different Epigenomic States in Single Mammalian Cells. Cell Rep 24, 873-882 (2018).
63. D. E. Olins, A. L. Olins, Epichromatin and chromomeres: a 'fuzzy' perspective. Open Biol 8 (2018).
64. D. G. Booth et al., 3D-CLEM Reveals that a Major Portion of Mitotic Chromosomes Is Not Chromatin. Mol Cell 64, 790-802 (2016).
65. A. A. Van Hooser, P. Yuh, R. Heald, The perichromosomal layer. Chromosoma 114, 377-388 (2005).
66. L. Stenstrom et al., Mapping the nucleolar proteome reveals a spatiotemporal organization related to intrinsic protein disorder. Mol Syst Biol 16, e9469 (2020).
67. S. Sazer, M. Lynch, D. Needleman, Deciphering the evolutionary history of open and closed mitosis. Curr Biol 24, R1099-1103 (2014).
68. D. Zhang, S. Oliferenko, Remodeling the nuclear membrane during closed mitosis. Curr Opin Cell Biol 25, 142-148 (2013).
69. S. Son et al., Resonant microchannel volume and mass measurements show that suspended cells swell during mitosis. J Cell Biol 211, 757-763 (2015).
70. E. Zlotek-Zlotkiewicz, S. Monnier, G. Cappello, M. Le Berre, M. Piel, Optical volume and mass measurements show that mammalian cells swell during mitosis. J Cell Biol 211, 765-774 (2015).
71. J. K. Eykelenboom et al., Live imaging of marked chromosome regions reveals their dynamic resolution and compaction in mitosis. J Cell Biol 218, 1531-1552 (2019).
72. T. J. Morikawa et al., Dependence of fluorescent protein brightness on protein concentration in solution and enhancement of it. Sci Rep 6, 22342 (2016).

73. T.-K. Kim et al., Mitotic Chromosomes in Live Cells Characterized Using High-Speed and Label-Free Optical Diffraction Tomography. Cells 8, 1368 (2019).
74. A. Yesbolatova et al., The auxin-inducible degron 2 technology provides sharp degradation control in yeast, mammalian cells, and mice. Nat Commun 11, 5701 (2020).
75. T. Natsume, T. Kiyomitsu, Y. Saga, M. T. Kanemaki, Rapid Protein Depletion in Human Cells by Auxin-Inducible Degron Tagging with Short Homology Donors. Cell Rep 15, 210-218 (2016).
76. K. Maeshima et al., Nuclear pore formation but not nuclear growth is governed by cyclin-dependent kinases (Cdks) during interphase. Nat Struct Mol Biol 17, 1065-1071 (2010).
77. S. Ide, R. Imai, H. Ochi, K. Maeshima, Transcriptional suppression of ribosomal DNA with phase separation. Sci Adv 6 (2020).
78. K. Ura, Y. Kaneda, Reconstitution of chromatin in vitro. Methods Mol Biol 181, 309-325 (2001).

Figures

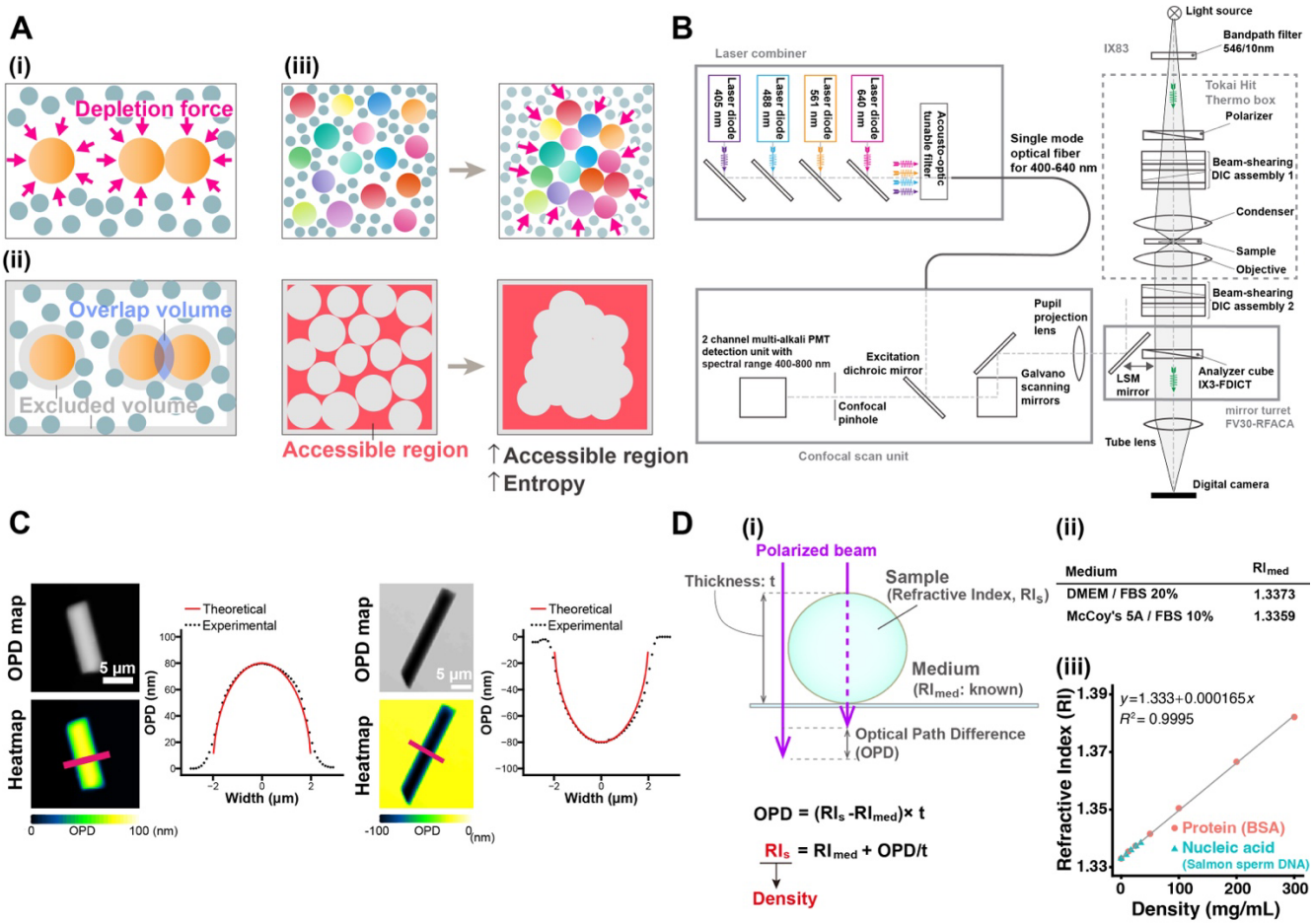

Figure 1.

Schematics of macromolecular crowding effect/depletion force, OI-DIC microscopy, and density quantification.

(A) (i) Many small spheres (blue-gray) representing soluble macromolecules bombard three large spheres (orange), representing chromatin, from all sides (arrows). When two large spheres come into contact (right), the small ones exert a force equivalent to their osmotic pressure on opposite sides of the two large ones to keep them together (macromolecular crowding effect/depletion force). (ii) The shaded regions in this alternative view show regions inaccessible to the centers of mass of the small spheres (excluded volumes). When two large spheres contact each other, their excluded volumes overlap and increase the volume accessible to the small spheres. Aggregation of the large spheres is then favored by an increase in the entropy of the system. (iii) Chromatin condensation by macromolecular crowding/depletion force. Chromatin domains/globules (colored spheres) are present in a square. The excluded volume is shown in gray. If chromatin domains associate with each other, the accessible region for soluble macromolecules (red) increases (excluded volume decreases). This state is then favored. **(B)** Optical schematic of confocal laser

scanning microscope Olympus FV3000 equipped with OI-DIC module. Details of the microcopy system are described under Materials and Methods. **(C)** Validation of density imaging by OI-DIC microscopy using known glass rods and mineral oils. The RI of the glass rods was 1.56, and those of the oils were 1.54 (left) and 1.58 (right). Note that the theoretical and experimental values are almost the same, ensuring the accuracy of our RI quantification. Scale bar: 5 μm. **(D)** (i) A procedure for estimating the RI of sample (depicted as a sphere). Our OI-DIC microscopy can computationally quantify optical path differences (OPDs) at each spatial point. For details, see Materials and Methods. (ii) The RI of medium measured by the refractometer. (iii) The calibration curve of RI versus the density of standard solutions for protein or nucleic acid. RI = $1.333 + 1.65 \times 10^{-4} \times C$ (RI, the refractive index; C, the concentration of the proteins or nucleic acids [mg/mL]). For details, see Materials and Methods.

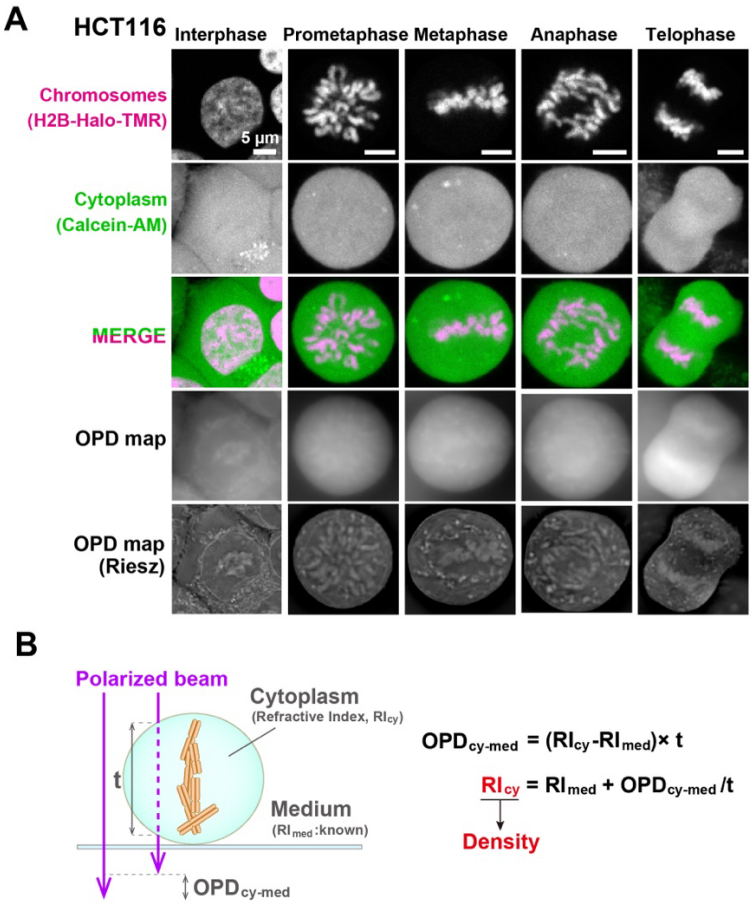

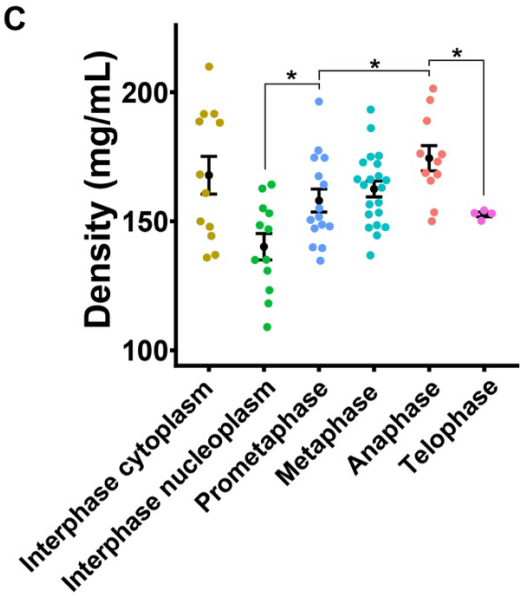

HCT116 cells	Density (mg/mL)
Interphase cytoplasm	174 ± 33.4
Interphase nucleoplasm	136 ± 23.2
Prometaphase cytoplasm	158 ± 17.2
Metaphase cytoplasm	163 ± 14.1
Anaphase cytoplasm	174 ± 16.2
Telophase cytoplasm	153 ± 1.73

Nucleolus: ~211 mg/mL (data from Fig. S3)

Figure 2.
Density imaging of live human HCT116 cells by the new OI-DIC microscopy.

(A) Confocal images of chromosome staining and cytoplasm staining, and OPD map and Riesz images obtained from OI-DIC imaging in live HCT116 cells. Riesz images are edge-enhanced OPD maps according to the inverse Riesz transform. To stain chromosomes, histone H2B-HaloTag was expressed in HCT116 cells and labeled with HaloTag ligand TMR. Cytoplasm was stained by Calcein-AM. Note that image intensities are not presented on the same scale for better visualization. Scale bar: 5 μm. **(B)** A simple schematic of the method to estimate the RI of cytoplasm (RI_{cy}). The RI_{cy} can be calculated using the formula shown based on the OPD measured by OI-DIC, the RI of medium (RI_{med}) measured by the refractometer, and thickness (t) values. For details, see Materials and Methods. **(C)** Total molecular densities of chromosome milieu gradually increased with the progression from prometaphase to anaphase in live HCT116 cells. Each dot represents the average of the estimated total density at several points within a single cell, where no apparent structure is apparent in the Riesz image (e.g., Fig. S4A). For details, see Materials and Methods. Black dots show the mean, error bars indicate the SE, and cell number are N = 13 (Interphase cytoplasm), N = 13 (Interphase nucleoplasm), N = 15

(Prometaphase cytoplasm), N = 21 (Metaphase cytoplasm), N = 11 (Anaphase cytoplasm), and N = 4 (Telophase cytoplasm). *, $P < 0.05$ by the two-sided unpaired t-test for Interphase nucleus vs. Prometaphase cytoplasm ($P = 9.5 \times 10^{-3}$), for Prometaphase cytoplasm vs. Anaphase cytoplasm ($P = 2.1 \times 10^{-2}$), for Anaphase cytoplasm vs. Telophase cytoplasm ($P = 1.2 \times 10^{-3}$).

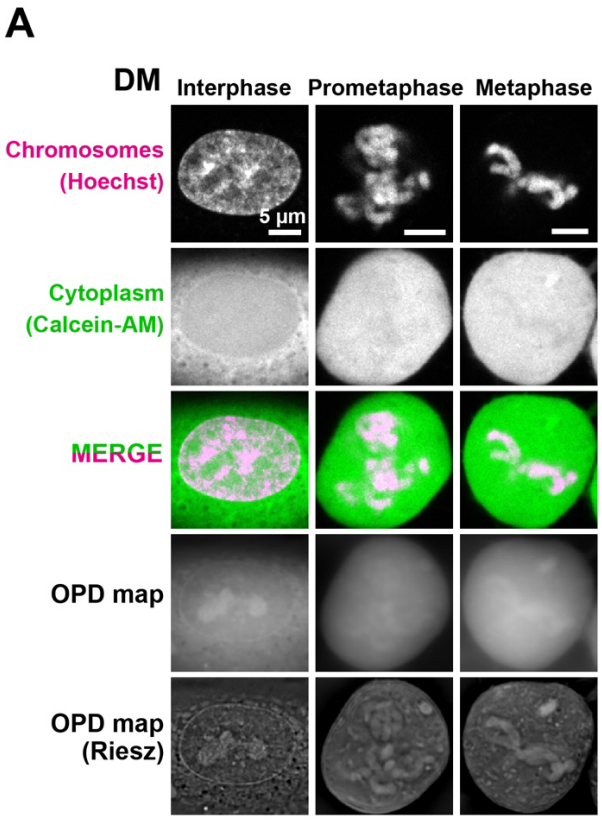

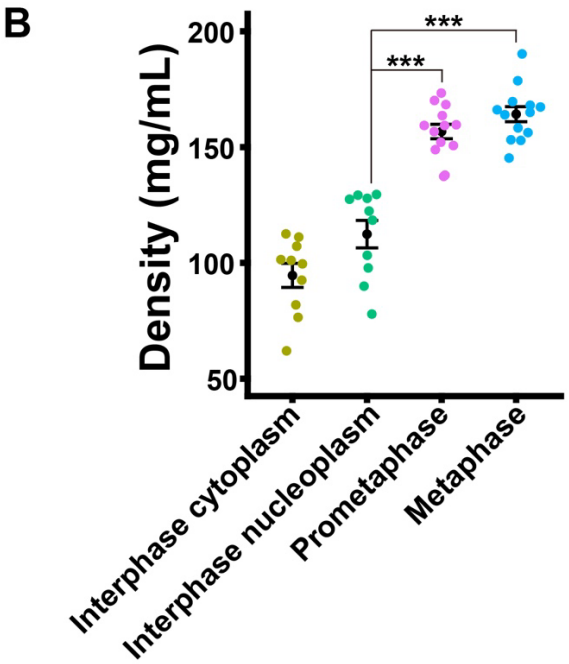

DM cells	Density (mg/mL)
Interphase cytoplasm	94.6 ± 16.4
Interphase nucleoplasm	112 ± 18.9
Prometaphase cytoplasm	156 ± 11.2
Metaphase cytoplasm	164 ± 11.7
Metaphase chromosome	185 ± 18.9

Figure 3.

Density imaging of live Indian Muntjac DM cells by the new OI-DIC microscopy.

(A) Confocal images of chromosome staining and cytoplasm staining, and OPD map and Riesz images obtained from OI-DIC imaging in live DM cells. Riesz images are edge-enhanced OPD maps according to the inverse Riesz transform. Chromosomes were stained with Hoechst 33342. Cytoplasm was stained by Calcein-AM. Note that image intensities are not presented on the same scale for better visualization. Scale bar: 5 µm. **(B)** Total molecular densities of chromosome milieu increased during mitosis in live DM cells. Each dot represents the average of the estimated total density at several points within a single cell, where no clear structure is apparent in the Riesz image. Black dots show the mean, error bars indicate the SE and cell numbers are N = 10 (Interphase cytoplasm), N = 10 (Interphase nucleoplasm), N = 13 (Prometaphase cytoplasm), and N = 13 (Metaphase cytoplasm). ***, $P < 0.0001$ by the two-sided unpaired t-test for

Interphase nucleus vs Prometaphase cytoplasm ($P = 9.5 \times 10^{-3}$) and for Interphase nucleus vs Prometaphase cytoplasm ($P = 2.1 \times 10^{-2}$).

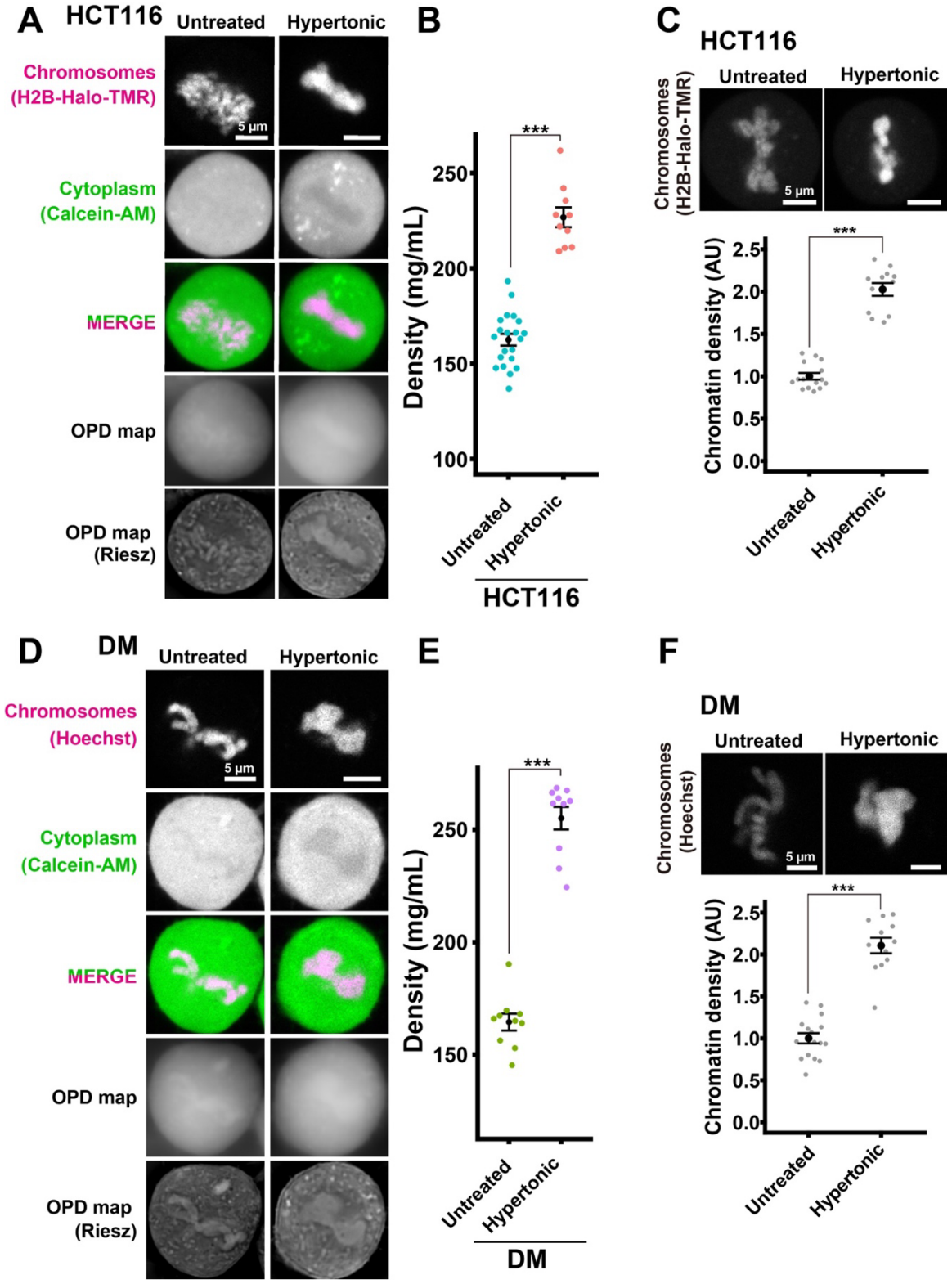

Figure 4.

Density imaging of hypertonic mitotic cells by the new OI-DIC microscopy.

(A) Confocal images of live HCT116 cells with hypertonic treatment, OPD map, and Riesz images obtained from OI-DIC imaging. Hypertonic treatment induced hypercondensation of chromosomes, making chromosomes fuse together. Chromosomes were labeled with histone H2B-HaloTag-TMR. Cytoplasm was stained by Calcein-AM. Note that image intensities are not presented on the same scale for visualization. Scale bar: 5 μm. **(B)** Hypertonic treatment increased the total densities of cytoplasm in mitotic live HCT116 cells. Each dot represents the average of the estimated total density at several points within a single cell, where no apparent structure is apparent in the Riesz image. Black dots show the mean, error bars represent the SE, and cell numbers are N = 21 (Untreated) and N = 10 (Hypertonic). ***, $P < 0.0001$ by the two-sided unpaired t-test ($P = 1.5 \times 10^{-8}$). Untreated data was reproduced from Fig. 2C (metaphase). **(C)** (Top) Hypertonic treatment induced hypercondensation of chromosomes of HCT116. Projection of 3 z-sections. Scale bar: 5 μm. (Bottom) Quantification of chromatin density in HCT116 cells with hypertonic treatment. Each dot represents the mean intensity of chromosome staining within a single cell, normalized by the mean intensity of untreated cells. Black dots show the mean, error bars represent the SE, and cell numbers are N = 15 (Untreated) and N = 15 (Hypertonic). ***, $P < 0.0001$ by Wilcoxon rank sum test ($P = 1.3 \times 10^{-8}$). AU, arbitrary units**. (D)** Confocal images of live DM cells with hypertonic treatment, OPD map, and Riesz images obtained from OI-DIC imaging. Hypertonic treatment induced hypercondensation of chromosomes, making chromosomes clump together. Chromosomes were stained with Hoechst 33342. Cytoplasm was stained by Calcein-AM. Note that image intensities are not presented on the same scale for visualization. Scale bar: 5 μm. **(E)** Hypertonic treatment increased the total densities of cytoplasm in mitotic live DM cells. Each dot represents the average of the estimated total density at several points within a single cell, where no clear structure is apparent in the Riesz image. Black dots show the mean, error bars represent the SE, and cell numbers are N = 10 (Untreated) and N = 10 (Hypertonic). ***, $P < 0.0001$ by the two-sided unpaired t-test ($P = 8.1 \times 10-11$). **(F)** (Top) Hypertonic treatment induced hypercondensation of chromosomes in DM cells. Projection of 3 z-sections. Scale bar: 5 μm. (Bottom) Quantification of chromatin density in DM cells with hypertonic treatment. Each dot represents the mean intensity of DNA staining within a single cell, normalized by the mean intensity of untreated cells. Black dots show the mean, error bars represent the SE, and cell numbers are N = 16 (Untreated) and N = 16 (Hypertonic). ***, $P < 0.0001$ by Wilcoxon rank sum test ($P = 1.3 \times 10^{-8}$). AU, arbitrary units.

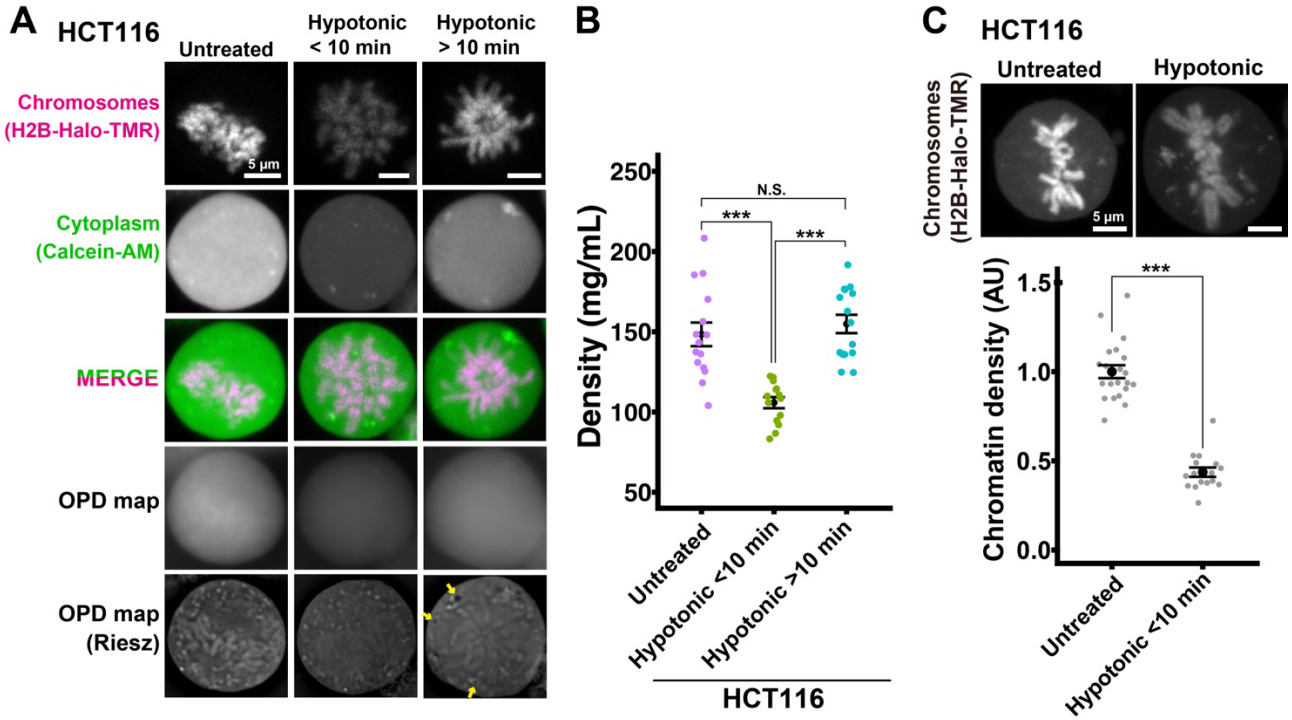

Figure 5.
Density imaging of hypotonic mitotic HCT116 cells by OI-DIC microscopy.

(A) Confocal images of live HCT116 cells with hypotonic treatment and OPD map and Riesz images obtained from OI-DIC imaging. Hypotonic treatment induced a transient decondensation of chromosomes (within 10 min after treatment), and then the chromosomes seemed to re-condense. Chromosomes were labeled with H2B-HaloTag-TMR. Cytoplasm was stained by Calcein-AM. Note that image intensities are not presented on the same scale for visualization. Scale bar: 5 µm. **(B)** Hypotonic treatment decreased the total densities of cytoplasm in mitotic live HCT116 cells. Each dot represents the measured points in multiple cells, where no structure was apparent in the Riesz image. Black dots show the mean, error bars represent the SE, and measured points are N = 15 (Untreated), N = 14 (Hypotonic < 10 min), and N = 15 (Hypotonic > 10 min). ***, $P < 0.0001$ by the two-sided unpaired t-test for Untreated vs Hypotonic < 10 min ($P = 3.5 \times 10^{-4}$) and for Hypotonic < 10 min vs Hypotonic > 10 min ($P = 1.9 \times 10^{-7}$). N.S., not significant ($P = 0.54$). **(C)** (Top) Hypotonic treatment (< 10 min) induced decondensation of chromosomes of HCT116. Projection of 3 z-sections. Scale bar: 5 µm. (Bottom) Quantification of chromatin density in HCT116 cells with hypotonic treatment (< 10 min). Each dot represents the mean intensity of DNA staining within a single cell, normalized by the mean intensity of untreated cells. Black dots show the mean, error bars represent the SE, and the cell numbers are N = 21

(Untreated) and N = 16 (Hypotonic). ***, $P < 0.0001$ by Wilcoxon rank sum test ($P = 1.6 \times 10^{-10}$). AU, arbitrary units.

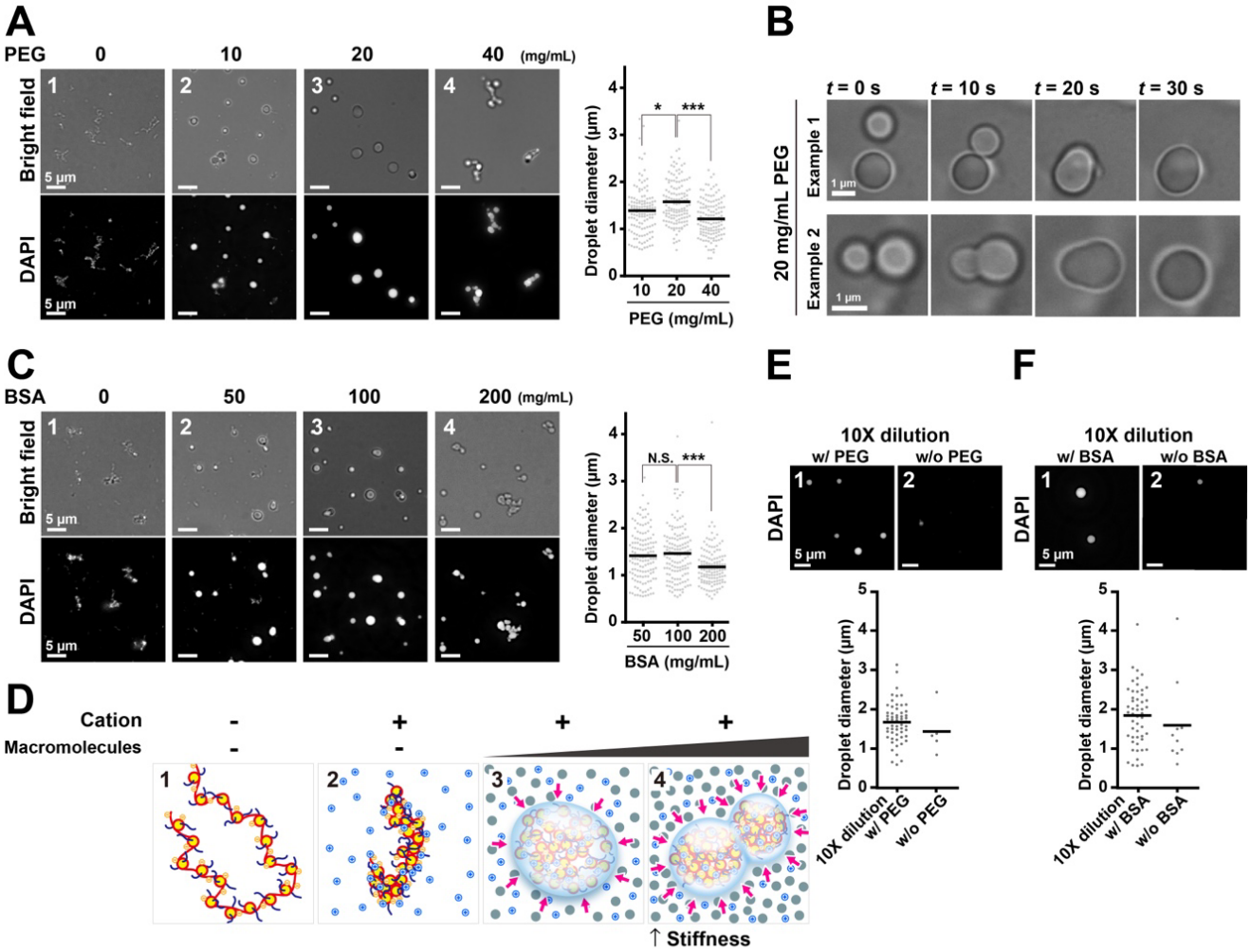

Figure 6.

Liquid droplet formation and solidification of chicken native chromatin by macromolecular crowders.

(A) Fibrous chromatin condensates were induced by 100 mM K^+ and 0.8 mM Mg^{2+} (Panel 1, 0 mg/mL PEG). PEG converted the fibrous condensates into droplets (Panels 2 and 3). Further increases in the concentration of PEG put the droplets together without fusions, suggesting the solid-like property of the droplets (Panel 4). Diameters of formed droplets were shown on the right plots. *, $P < 0.05$ by Wilcoxon rank sum test for 10 mg/mL vs. 20 mg/mL PEG ($P = 0.011$). ***, $P < 0.0001$ for 20 mg/mL vs. 40 mg/mL PEG ($P = 7.5 \times 10^{-9}$). **(B)** Fusions of formed droplets. Two typical examples are shown. Also see Movie S1. **(C)** Similar analyses to (A) on BSA-induced liquid droplets. N.S., not significant by Wilcoxon rank sum test for 50 mg/mL vs. 100 mg/mL BSA ($P = 0.78$). ***, $P < 0.0001$ for 100 mg/mL vs. 200 mg/mL BSA ($P = 7.0 \times 10^{-6}$). **(D)** Schematics of conversion from fibrous chromatin condensates to liquid droplets. The chromatin is stretched

by electrostatic repulsion without cations (Panel 1). Mg^{2+} and K^{+} decrease net negative charge and repulsion and induce fibrous chromatin condensates (Panel 2). Macromolecular crowding/ depletion force converts the fibrous condensates into droplets (Panel 3). Further crowding makes the droplets stiffer (Panel 4). **(E)** The droplet dilution assay. After the droplets were formed with 20 mg/mL of PEG, the reaction mixtures were diluted 10-fold in a buffer with (Panel 1) or without (Panel 2) 20 mg/mL of PEG. The images depict fewer and smaller droplets in the diluted buffer without PEG, suggesting that the droplets were dissolved in the diluted buffer. (Bottom) A quantitative analysis of the droplet dilution assay. The number and diameters of the droplets in a randomly picked area (6.0×10^4 μm^2) are plotted. **(F)** The dilution assay on BSA-formed droplets.

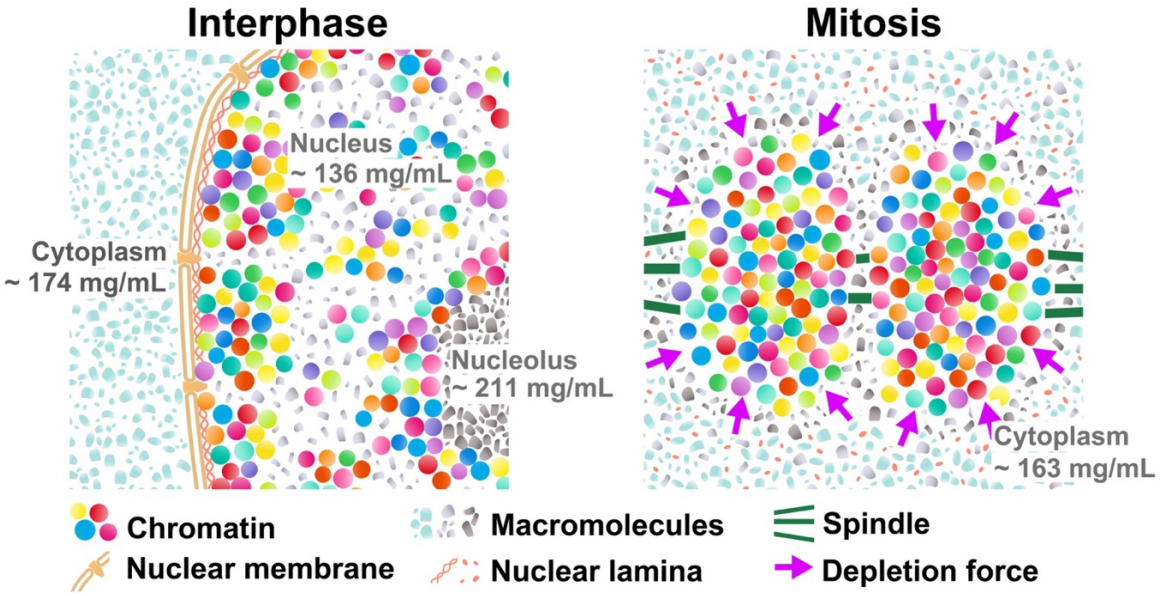

Figure 7.

Model for upregulation of macromolecular crowding in mitotic cells.

(Left) Schematic of macromolecular crowding in interphase live cells with soluble macromolecules in cytoplasm (light-blue), nucleoplasm (gray), and nucleolus (dark gray). The cytoplasm, nucleus, and nucleolus are compartmentalized and not mixed during interphase. Molecular densities of nucleoplasm are lower than the cytoplasm and nucleolus. (Right) After NEBD, soluble macromolecules that were localized to the cytoplasm, nucleus, and nucleolus at interphase are now mixed. Molecular density of chromosome milieu increases, making the macromolecular crowding effect stronger, and contributes to local condensation of chromosomes. Note that these are highly simplified models.